PHYSICAL REVIEW MATERIALS **4**, 123801 (2020)

Hierarchical morphologies in co-sputter deposited thin films

Max Powers,[1,*] Benjamin Derby,[2] Sudeep Nerlige Manjunath,[1] and Amit Misra[1]

[1]*Department of Material Science and Engineering, University of Michigan, 2300 Hayward St., Ann Arbor, Michigan 48109, USA*

[2]*Los Alamos National Laboratory, Los Alamos, New Mexico, USA*

(Received 3 October 2020; accepted 30 November 2020; published 17 December 2020)

Co-depositions of immiscible alloy films at specific processing conditions have yielded hierarchical microstructures which consist of distinct features at multiple length scales, often agglomerates and concentration modulations on the submicrometer scale and fine nanoprecipitates in a matrix on the nanoscale. The present work examined a series of immiscible alloy systems: Cu-Mo, Cu-Ag, Cu-Fe, Cu-Ta, Mo-Ag, Cu-Mo-Ag, to determine the kinetic conditions favorable for hierarchical organization and the formation mechanism of such structures. Thin films of six immiscible systems were sputter co-deposited over a range of deposition rates from 0.12 to 2 nm/s and various temperatures from 400 to 800°C. The resulting microstructures indicate that hierarchical structures form with sufficient disparity in kinetic energy between the constituent atoms, one species being highly mobile (*A*) and the other relatively immobile (*B*). This condition arises typically at elevated deposition temperatures and reduced deposition rates but is also alloy dependent. The hierarchical structures form during deposition via phase separation and self-organization processes across the multiple length scales. The adatoms diffuse on the film surface with the highly mobile species swiftly agglomerating into *A*-rich domains within which *B*-rich nanoprecipitates form, often self-organizing into periodic arrays. The smallest *B*-rich nanoprecipitates in the *A*-rich domains are found to be coherent and in a metastable crystal structure (*B* taking the structure of *A*), but coarser precipitates exhibit the equilibrium structure of the *B* element. The *A*-rich domains are surrounded by a *B*-rich matrix that phase-separates into a concentration modulated structure. The observations are interpreted via a model incorporating material properties and process parameters.

DOI: 10.1103/PhysRevMaterials.4.123801

I. INTRODUCTION

A hierarchical microstructure has distinct phases and morphologies at multiple length scales, differing from a bimodal structure in which the same characteristic (e.g., equiaxed grains of the same phase) is emulated across two length scales [1]. With their complex multilength-scale structures that may include nonequilibrium states, hierarchical architectures have a wide range of applications in electrochemical processes [2] and as functional materials [3]. Recent work has shown these hierarchical morphologies may self-assemble during the magnetron co-sputtering of immiscible metallic alloy films [4–8]. There is extensive evidence that heterogeneous films may exhibit advantageous physical properties such as high strength and corrosion resistance [4], suppression of shear banding [5], enhanced strength and fracture toughness [6], and prominent radiation tolerance [7]. However, there is limited fundamental understanding as to the formation mechanisms of hierarchical features in immiscible alloy thin films due to self-organization during deposition.

It is well understood that immiscible elements co-deposited using physical vapor deposition (PVD) will self-organize into phase-separated regions with chemically sharp interfaces [8]. The self-organization and mutual immiscibility may stem from a positive enthalpy of mixing, an equilibrium phase difference, e.g., fcc for one element and bcc for the other, disparate lattice parameters, or a combination of the three. Previous work has emphasized homogeneous microstructure formation within immiscible alloy films, where homogeneous refers to a constant concentration modulation wavelength and morphology throughout the sample. Systems such as Cu-W [9,10], Cu-Ta [11,12], and Cu-Mo [13] have yielded concentration modulation structures whose specific orientations can be controlled by varying the PVD processing parameters. The homogeneous co-deposited microstructures are categorized into three quintessential morphologies: vertical concentration modulation (VCM), lateral concentration modulation (LCM), and random concentration modulation (RCM) structures. To assist with the visualization of the two microstructures, Fig. 1 provides cartoons of a generic homogeneous structure, Fig. 1(a), and a generic heterogeneous hierarchical structure, Fig. 1(b).

The concentration modulations refer to alternating regions rich in one constituent element. The kinetics of formation describing these homogeneous structures can be described with an empirical relationship relating elemental interdiffusion length of the landing deposited atoms (adatoms) to deposition flux, surface interdiffusivity, and width of the surface layer [14,15]. The formation mechanism is further elucidated by incorporating the influence of processing parameters on thin film growth [16] and considering the thermodynamics of phase separation. Indeed, multiple phase-field models have successfully demonstrated the formation

---

[*] Corresponding author: maxpow@umich.edu

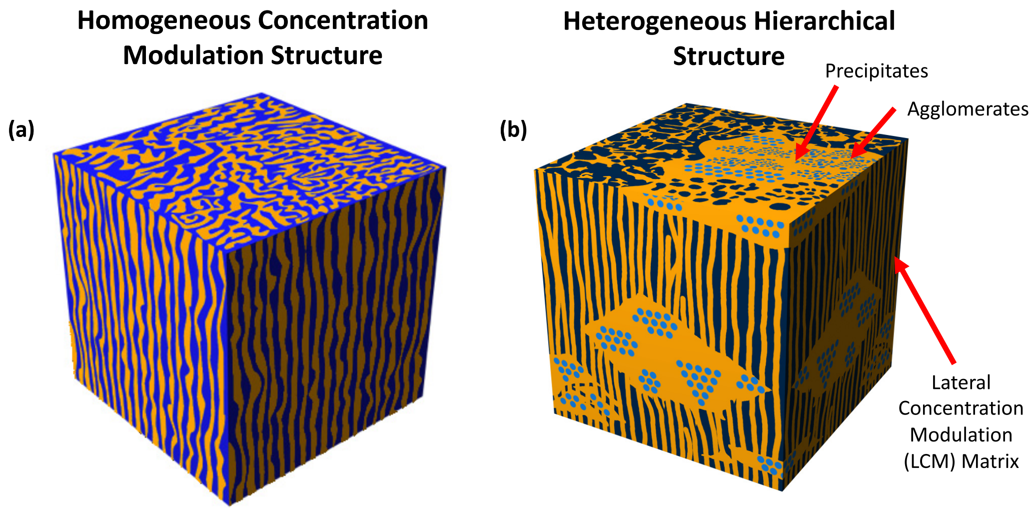

FIG. 1. Cartoon visualization of the (a) homogeneous structure and (b) heterogeneous hierarchical structure.

mechanisms of the concentration modulation structures in thin films [17–19].

The model for homogeneous morphologies is insufficient in describing the development of hierarchical film microstructures. Individual elemental interdiffusion length does not account for the formation of agglomerates with precipitates depicted in Fig. 1(b). Additionally, the presence of pseudomorphism within hierarchical structures points to thermodynamic free-energy potentials that are more complex than previously considered. Psuedomorphism refers to localized metastable free energy minima that result in far-from-equilibrium structures, e.g., fcc structure in Mo-rich nanoprecipitates in Cu matrix [8]. The microstructure suggests that multiple global and local energy minima are present rather than the simple free energy double well potential commonly used to represent spinodal decomposition. This is coupled with interfacial and lattice coherency energies driving the fine-scale microstructure evolution in a manner that warrants further investigation. Certain molecular dynamics [18] and *ab initio* [8] calculations have explored the interface formation and metastability of phases during the phase separation process. A hierarchical morphology suggests that the atomic species are following multiple kinetic pathways during film deposition. The precise kinetic pathways for hierarchical morphology formation during film growth are unclear, although it should be noted that hierarchical structures can also form due to multistep solid-state phase transformations in bulk systems, e.g., $(\alpha + \beta)$ Ti alloys [20].

For the case of thin films, both Cu-Mo [8] and Cu-Ta [21] exhibited hierarchical structures when co-sputtered at deposition temperatures exceeding 600°C at low deposition rates. The constituent elements were present in both equilibrium and pseudomorphic phases. The Cu-Mo structure contained large Cu-rich agglomerates (∼100 nm diameter) and fine fcc Mo precipitates with the agglomerates surrounded by a coherent Cu-Mo bcc LCM matrix. The Cu-Ta structure displayed trace Ta particles inside of Cu-rich agglomerations all encompassed by Ta-rich veins. Current mesoscale simulation work [17–19] on co-deposition of immiscible alloys is unable to accurately depict the simultaneous progression of distinct features across multiple length scales reported experimentally in co-deposited PVD films of immiscible elements.

The emphasis of the current work is to probe various systems of co-deposited immiscible alloys to identify the processing conditions and material properties that lead to hierarchical morphologies. The work of Atzmon [14] and Adams [22] provides an important context for the results especially the conclusion that surface diffusion is the prominent method of material transport in a depositing film. The present experiments will help answer the question: why do hierarchical structures exist in some co-deposited systems but not others? Cu-W deposited at room temperature then annealed at 750°C will coarsen from a solid-solution to form interpenetrating bicontinuous networks but not a hierarchical morphology [23]. Even within the binary alloy of Cu-Ta, metallic thin films fabricated in comparable processing conditions as Ref. [21] did not exhibit the trademark distinct features across multiple length scales. Interestingly, experiments for Cu-Ta films co-sputtered at room temperature that varied the Ta content [24] and induced a Ta phase transformation from metastable β-Ta to equilibrium α-Ta with a heat treatment [25] did not result in a hierarchical structure.

A series of fcc-bcc immiscible alloys: Cu-Mo, Cu-Ag, Cu-Fe, Cu-Ta, Mo-Ag, Cu-Mo-Ag, were co-deposited and characterized to determine the processing parameters and elemental properties that could lead to hierarchical morphologies. The six systems represent a spectrum of elemental properties during phase-separated thin film growth to gauge the effect of the parameters of relative elemental interdiffusion length, the deposition rate, and increased deposition temperature. The resultant film microstructures will also elucidate the formation mechanisms that enable disparate phase-evolution on the micro- and nanoscale.

II. EXPERIMENTAL METHODS

A. Fabrication and co-deposition

All thin films were co-deposited onto thermally oxidized Si substrates by DC magnetron sputtering in a Kurt J Lesker PVD 75 deposition system. The substrates were

TABLE I. List of samples fabricated with respective processing temperatures and deposition.

	300°C	400°C	600°C	800°C
Cu-Mo		X	X,Y	X
Cu-Ag			X,Y	
Cu-Fe	Z			
Cu-Ta		W	W	W
Mo-Ag			X,Y	
Cu-Mo-Ag		V	V	V
$X = 0.12$ nm/s, $Y = 1.4$ nm/s, $Z = 0.48$ nm/s, $W = 0.15$ nm/s, $V = 2$ nm/s				

3-in.-diameter Si with a 1000-nm-thick SiO_2 surface layer. Before deposition, the substrates were ultrasonically cleaned in acetone, rinsed with isoproponal alcohol, and dried with filtered compressed air. Five different 2-in.-diameter targets were used (Cu, Mo, Ag, Fe, Ta), all with at least 99.95% purity, for the various combinations of the binary and ternary alloys. The targets were oriented confocally with a 5-in. throw distance towards a rotating substrate at 10 rpm. The sputtering occurs in a vertical direction with the targets depositing material upwards onto the substrates. Base pressure in the chamber prior to sputtering was less than 2.7×10^{-5} Pa. The process gas was Ar which was maintained at a pressure of 0.4 Pa during operation. Precise deposition rates were governed by controlling the DC power supplied to each target. For any film fabrication at an elevated deposition temperature, a substrate heater resistor coil would heat and maintain a requisite temperature throughout the deposition period. The deposition temperature was monitored with a thermocouple located between the heater and the substrate.

The binary alloy pairings, Cu-Mo, Cu-Ag, Cu-Fe, Cu-Ta, Mo-Ag, were sputtered with nominally equiatomic composition (e.g., 50 at.% for each element) to create bicontinuous morphologies of separating phases and avoid discrete particle development of a minority phase. The ternary alloy, Cu-Mo-Ag, had a 33.3 at.% composition for each element. The bulk composition of the alloy films was confirmed via x-ray fluorescence (XRF) spectroscopy using a Rigaku Supermini200. Accurate compositions were verified by targeting the appropriate elemental peaks and applying Gaussian peak fitting to reduce noise. A variety of deposition rates and deposition temperatures were used to probe different kinetic conditions for phase-separated thin film growth. The various deposition conditions are detailed below. All noted deposition rates are a combined co-deposition rate for the respective alloy combinations.

A series of Cu-Mo films were deposited at 400, 600, and 800°C at a rate of 0.12 nm/s (see Table I). A second series of Cu-Mo was produced at 600°C at a rate of 1.4 nm/s. The Cu-Ag was fabricated at 600°C with one film at a rate of 0.12 nm/s and a second at 1.4 nm/s. The Cu-Fe was sputtered at 300°C with a rate of 0.48 nm/s. Cu-Ta was deposited at 400, 600, and 800°C at a rate of 0.15 nm/s. Mo-Ag was deposited at 600°C with one film at the rate 0.12 nm/s and a second at 1.4 nm/s. The Cu-Mo-Ag ternary was deposited at 400, 600, and 800°C at 2 nm/s. All films were deposited to a nominal 1 μm thickness with the exception of the Cu-Ta films whose thickness ranged from 700 nm to 1 μm due to coarse grains protruding from the film surface. Postdeposition, the films were left to cool to room temperature in the PVD chamber to inhibit surface oxide formation.

B. Characterization of films

Chemical and microstructural characterization was used to link the morphologies and the processing parameters. Scanning/transmission electron microscopy (S/TEM) foils were prepared using focused ion beam (FIB) milling techniques in a TFS Helios 650 Nanolab SEM/FIB and a TFS Nova 200 Nanolab SEM/FIB. The foils were lifted out and attached to either Si or Mo grids to prevent interference during chemical composition scans. After thinning, the samples were plasma cleaned for a period of 5–8 min prior to S/TEM characterization on two microscopes, JEOL 3100R05 double-Cs corrected S/TEM and JEOL 200 C-ARM. The JEOL 3100 R05 was operated at 300 keV to achieve a point-to-point resolution of 0.055 nm for high-angle annular darkfield (HAADF) and brightfield (BF) imaging. The convergent angle for all image collection 111° with a camera length of 8 cm to true Z-contrast HAADF imaging. Energy dispersive x-ray spectroscopy (EDS) compositional maps were collected using a JEOL SDD x-ray detector with a 60 mm^2 active area. The JEOL 200 C-ARM was similarly employed with a 200-keV working voltage.

III. RESULTS

A. Key kinetic parameters

As all the deposited immiscible systems have a similar phase-separating driving force, it is useful to frame the systems in terms of the kinetics of the adatoms arriving on the film surface. While the physical mechanisms that lead to phase separation in bulk materials also occur in films, the process is complicated by two factors as outlined by Atzmon *et al.* [13]: (1) deposition occurs at a fixed, externally imposed rate, and (2) atomic transport occurs preferentially along the advancing surface. The implication is that surface diffusion is the dominant mechanism for film material flux and phase separation at the temperatures relevant to the current experiment. The prevalence of surface diffusion stems from the elemental surface diffusivity being orders of magnitude higher than that for bulk diffusivity. In literature, Al-Ge films deposited at 375°C for half an hour yielded bulk interdiffusion lengths of ∼5 nm compared to surface interdiffusion lengths of ∼400 nm [14]. In the present case, a "frozen bulk" approximation may be applied in which any elemental bulk diffusion is minimal and nearly negligible for films deposited at lower

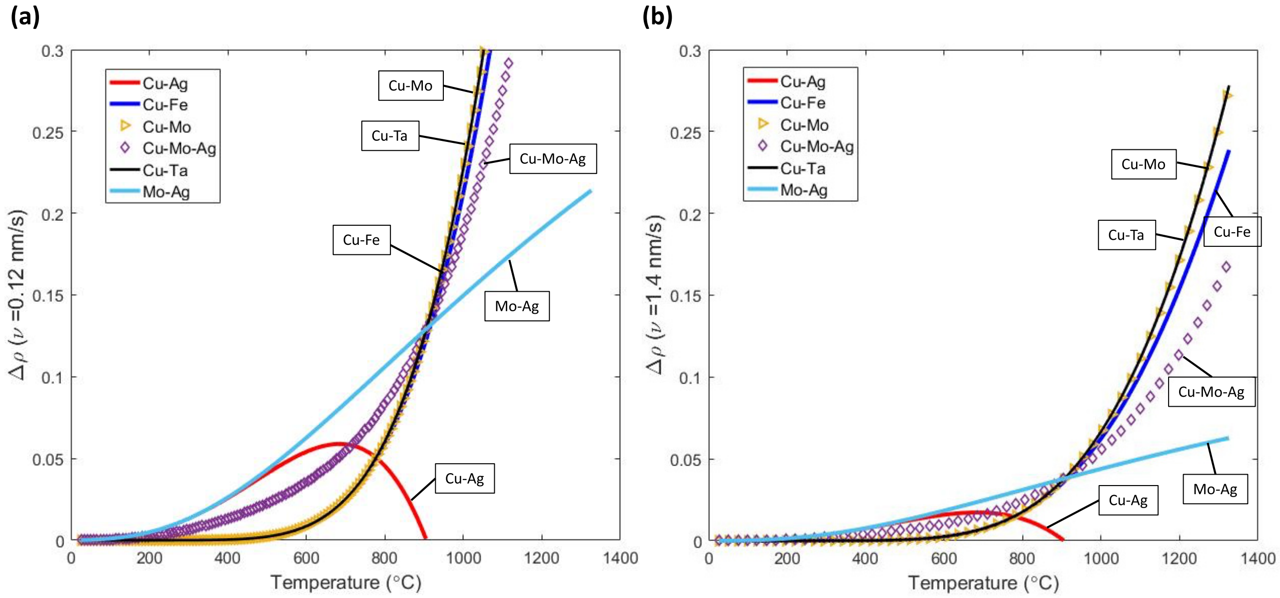

FIG. 2. The kinetic parameter $\Delta\rho$ as a function of deposition temperature for the deposition rates (a) $\nu = 0.12$ nm/s and (b) $\nu = 1.4$ nm/s for the six co-deposited immiscible alloy systems of the present experiment. The elevated deposition temperature increases $\Delta\rho$ for all systems but to different degrees.

temperatures. As deposition temperatures increase, the contribution of bulk diffusion to microstructure development becomes more significant especially for films sputtered at $T \geqslant 800\,^{\circ}$C. Additionally, the adatoms kinetics can be manipulated with variations in deposition rate and temperature. It is important to note that during magnetron sputtering the adatoms land on the substrate with a finite incident kinetic energy. The changes in processing deposition rate and temperature further add to the elevated kinetic energy.

An adatom may traverse a specific distance along the film surface before being buried under the oncoming material flux. The distance is termed the surface interdiffusion length ρ and is a consequential parameter for phase-separated morphologies. The Atzmon *et al.* model describes the surface interdiffusion length as

$$\rho = \sqrt{\frac{D_s\delta}{\nu}}, \tag{1}$$

where D_s is the surface diffusivity of the species, δ is the thickness of the most recently deposited layer (on the order of interatomic spacing), and ν is the deposition flux. Typically, the adatoms will locally demix to minimize system energy, which influences the subsequent layers, and grow into the homogeneous phase-separated regions. The deposition flux ν is in direct competition with the rate of phase separation as increases in ν equate to abbreviated surface interdiffusion lengths. The surface interdiffusion length and the mobility of an elemental adatom are related due to their mutual dependence on diffusivity [26].

Considering the surface interdiffusion length for an individual species is insufficient to explain the concurrent agglomeration and formation of concentration modulation depicted in Cu-Mo and Cu-Ta from literature [19,21]. Comparative systems with nearly identical surface interdiffusion lengths produced homogeneous morphologies in some instances and heterogeneous morphologies in others. Instead, we propose that a more accurate parameter is the difference in surface interdiffusion length for the constituent elements. The difference, $\Delta\rho$, is expressed as

$$\Delta\rho = \sqrt{\frac{(D_s)_A\delta}{\nu}} - \sqrt{\frac{(D_s)_B\delta}{\nu}}, \tag{2}$$

where δ and ν are consistent with Eq. (1). The surface diffusivity D_s is reliant on the species deposited, A or B, for the binary alloy. The surface diffusivity is given by the well-known expression [27]

$$D_s = D_0 \exp\left(\frac{-Q}{k_bT}\right), \tag{3}$$

where D_0 is a diffusivity coefficient, Q is the activation energy required for the movement of an atom to an available adjacent site, k_b is Boltzmann's constant [27], and T is temperature. Coupling Eqs. (2) and (3) reveals the sensitivity of $\Delta\rho$ to temperature and deposition rate which can both be varied as processing parameters.

Figure 2 plots the $\Delta\rho$ as a function of temperature at the distinct deposition rates of $\nu = 0.12$ and 1.4 nm/s for each of the six co-deposited elemental pairings. For the case of Cu-Mo-Ag, the average between the $\Delta\rho$ for Cu-Mo and Cu-Ag was used. Figure 2(a) shows that the immiscible alloy pairings fall into three kinetic regimes: (i) $\Delta\rho$ steadily increases at $T > 200$°C; (ii) $\Delta\rho$ is muted then rapidly increases at $T > 600$°C; (iii) $\Delta\rho$ increases at $T > 200$°C to a peak at ≈600°C, followed by a rapid decrease to $\Delta\rho$ value of zero. The three regimes can be explained by the relative surface mobilities as a function of temperature for the depositing elements. Regime (i) describes the Mo-Ag system in which both elements have the same proportional increase in surface mobility with respect to increasing temperatures. The regime (ii) alloys of Cu-Ta, Cu-Mo, Cu-Mo-Ag, and Cu-Fe follow a different

TABLE II. Homologous temperatures of deposited elements.

Deposition temperature	Cu	Ag	Fe	Mo	Ta
673 K	0.495	0.545	0.372	0.232	0.205
873 K	0.642	0.707	0.482	0.301	0.265
1073 K	0.789	0.869	0.592	0.371	0.592

pattern. As the deposition temperature exceeds 600°C, the surface interdiffusion length of Cu increases at a significantly higher rate than its complementary element which yields a swift escalation in $\Delta\rho$. In regime (iii) Cu-Ag the difference in surface interdiffusion length becomes pronounced above $T > 200°\text{C}$ in which Ag is significantly more mobile than Cu. However, at $T > 600°\text{C}$, both the Cu and Ag have nearly identical ρ which minimizes $\Delta\rho$ to zero.

Figure 2(b) reveals that increasing the deposition rate to 1.4 nm/s decreases the calculated $\Delta\rho$ for the co-deposited alloys and delays the onset for increased $\Delta\rho$ as a function of elevated temperature. The three kinetic regimes and respective behaviors are still present for the six immiscible systems but the steady increase in $\Delta\rho$ for regime (i) now initiates at 225°C, regime (ii) now exhibits a drastic increase at $T > 625°\text{C}$, and the peak and dip of regime (iii) are shifted by 25°C. Figure 2 demonstrates that a lower deposition rate and an elevated deposition temperature allot greater time for surface diffusion and facilitate the movement of a highly mobile species. The agglomeration of that highly mobile species will depend on the kinetic regime. From Fig. 2(a), regime (i) will likely form agglomerates with $T > 400°\text{C}$. For regime (ii), agglomeration appears likely with $T > 700°\text{C}$. In regime (iii), the temperature window for agglomeration is between 400 and 800°C. With an increased deposition rate in Fig. 2(b), agglomeration is only likely for regime (ii) at deposition temperatures exceeding 800°C.

Probabilities for agglomeration related to $\Delta\rho$ do not fully encompass the kinetics of hierarchical architectures. The influence of the deposition temperature on the movement of an individual species must also be considered. The direct impact of increased temperature on an element can be quantified with the homologous temperature T_H. The homologous temperature can be defined as

$$T_H = \frac{T_{\text{Deposition}}}{T_m}, \tag{4}$$

with $T_{\text{Deposition}}$ being the PVD processing temperature and T_m being the melting temperature of a specific element, in kelvin. Table II provides the T_H for the elements relevant to the current immiscible alloy systems. It is important to note that the adatoms of a species is considered highly mobile at $T_H > 0.35$. The $\Delta\rho$ and T_H create a kinetic threshold above which a hierarchical structure will likely form. Two conditions must be satisfied, the co-deposited immiscible alloy has a significant $\Delta\rho$ value and one element must be in the highly mobile T_H domain.

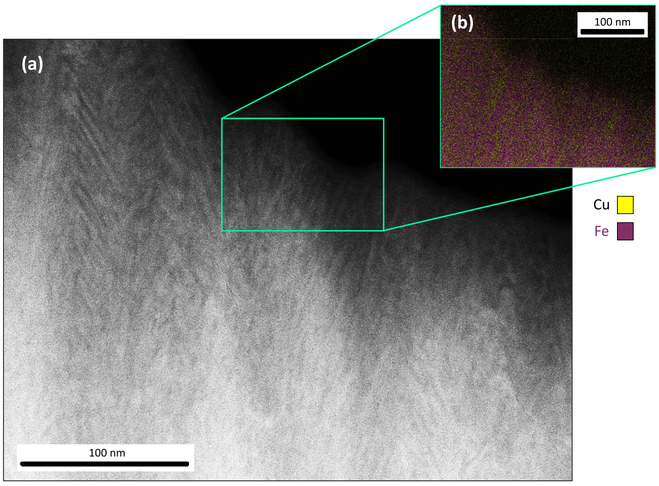

FIG. 3. (a) Scanning transmission electron microscopy (STEM) high-angle annular darkfield (HAADF) micrograph with atomic number contrast of Cu-Fe with homogeneous LCM morphology. (b) Energy dispersive x-ray spectroscopy (EDS) imaging of Cu-Fe demonstrating the alternating Cu-Fe layers.

B. Processing-microstructure relationship in immiscible alloy films

The fabricated thin films of the six immiscible alloys systems: Cu-Mo, Cu-Ag, Cu-Fe, Cu-Ta, Mo-Ag, Cu-Mo-Ag, contain either homogeneous phase-separated microstructure or heterogeneous hierarchical microstructure. Homogeneous, in the present context, is defined as a morphology described by phase-separated concentration modulations of a single length scale (e.g., a 10-nm wavelength from the start of the Cu-rich region to the end of the Ta-rich region). Figure 3 portrays a homogeneous morphology observed in Cu-Fe deposited at 300°C and 0.48 nm/sec. STEM-HAADF images in Fig. 3(a) show Cu and Fe self-assembled into Cu-rich and Fe-rich phase-separated regions, ~20 nm in width, organized into lateral concentration modulation (LCM). The EDS of Fig. 3(b) further demonstrates the alternating Cu-rich and Fe-rich regions. Planar imaging (not pictured) confirms the tortuous grains of Cu and Fe extending to the film surface. Figure 2(a) rationalizes the homogeneous morphology, as Cu-Fe under these processing conditions has a calculated $\Delta\rho$ of nearly zero.

In contrast, the heterogeneous hierarchical architectures display different features at various length scales in the film. STEM-HAADF images in Fig. 4 reveal that Cu-Ta deposited at 600°C and 0.15 nm/sec presents a hierarchical structure as it contains large Cu-rich domains, ~200–500 nm in size, surrounded by Ta-rich veins on the microscale but further examination of the Cu-rich regions show an interspersion of Ta clusters on the nanoscale. The Ta clusters are identified by high resolution HAADF images and corresponding FFTs, Fig. 4(b), indicating a Ta bcc crystalline structure. The hierarchical microstructure is explained by the calculated kinetic parameters. The co-sputtered Cu-Ta has $\Delta\rho = 0.0087$ and $T_H^{\text{Cu}} = 0.642$, $T_H^{\text{Ta}} = 0.265$. While $\Delta\rho$ is a reduced value, the homologous temperatures denote a highly mobile Cu and a relatively immobile Ta which favors the preferential

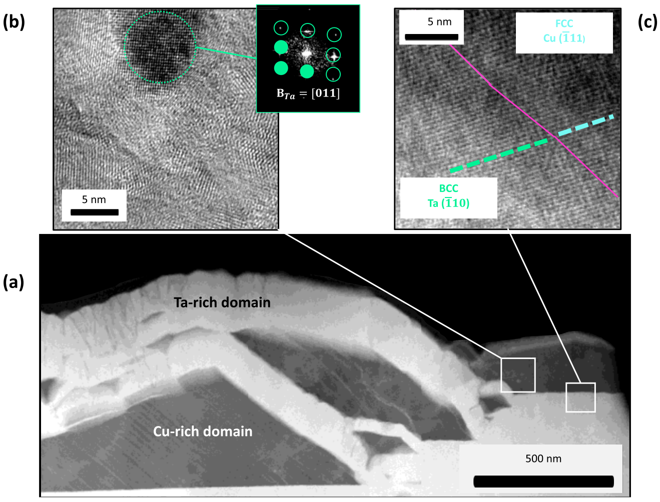

FIG. 4. (a) STEM-HAADF image of Cu-Ta with hierarchical microstructure morphology. Darker contrast regions are Cu-rich agglomerates which contain a minority of light contrast Ta precipitates. The agglomerates are surrounded by Ta-rich veins. (b) High resolution transmission electron microscopy (HR TEM) micrograph of the Cu agglomerate and incorporated Ta precipitate. The FFT of the encircled area confirms a bcc Ta structure. (c) HR TEM image of the Cu-rich agglomerate and Ta-rich vein interface. The Cu ($\bar{1}$11) plane aligns with the Ta ($\bar{1}$10) plane across the semicoherent interface.

agglomeration of Cu and leads to the observed morphology. Figures 3 and 4 provide general examples of homogeneous and hierarchical structures. From this point, the discussion will focus upon the underlying mechanisms and the conditions that give rise to hierarchical features in select co-deposited systems.

The processing parameters of deposition rate ν and the deposition temperature were varied to determine the influence of $\Delta\rho$ and T_H on the resultant microstructure within an alloy system and comparatively across multiple alloy systems. Figure 5 presents HAADF STEM images of Cu-Mo deposited at $\nu = 0.12$ nm/s and $\nu = 1.4$ nm/s both at 600°C. The micrographs show hierarchical structure at low ν and homogeneous lateral concentration modulation at higher ν. Although the T_H is constant between Figs. 5(a) and 5(b), lowering ν by an order of magnitude yields a threefold increase in $\Delta\rho$, from 0.0025 to 0.0087. The elevated $\Delta\rho$ for Cu-Mo in Fig. 5(a) thereby surpasses a kinetic threshold for difference in surface interdiffusion length and presents a heterogeneous morphology.

Figure 6 shows HAADF STEM, HR TEM, FFTs, and EDS images of Cu-Mo films co-deposited at 400, 600, and 800°C with $\nu = 0.12$ nm/s. Phase contrast within the HAADF images depict large Cu-rich agglomerates surrounded by Cu-Mo bicontinuous matrix for the three films. The presence of a hierarchical structure at 400°C despite a lower $\Delta\rho$ value validates the hypothesis that multiple variables contribute the immiscible alloy thin film kinetics. The agglomeration behavior for Cu is expected as it is highly mobile at 400, 600, and 800°C [28] with $T_H^{\mathrm{Cu}} = 0.495$, 0.642, and 0.789 respectively. The Mo is relatively immobile, reaching moderate mobility only at 800°C with a T_H^{Mo} of 0.371. In all cases, the Cu-rich agglomerates contained Mo precipitates. The size and

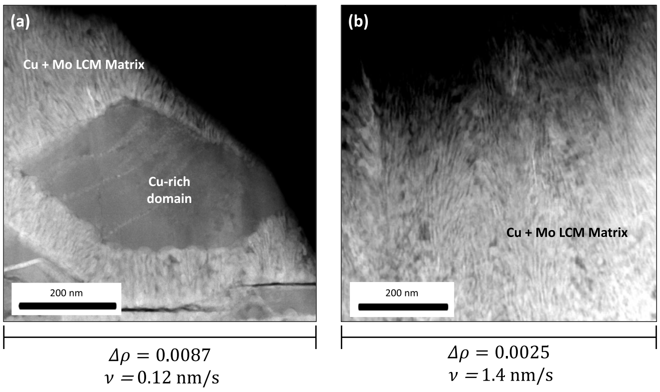

FIG. 5. STEM-HAADF images of Cu-Mo deposited in identical conditions except for deposition rate. (a) With $\nu = 0.12$ nm/s, the Cu-Mo self-segregated in a Cu-rich agglomerate surrounded by a Cu-Mo LCM matrix. (b) With $\nu = 1.4$ nm/s, the Cu-Mo formed solely a Cu-Mo LCM structure. Altering the deposition rate by an order of magnitude and subsequentially altering $\Delta\rho$ yielded significant morphological change from a hierarchical to a homogeneous structure.

nature of the Mo precipitates varied with respect to deposition temperature as elevated temperature led to feature coarsening and a change in crystal structure. Figure 6(a) reveals that the 400°C film has pseudomorphic fcc-Mo precipitates which are energetically preferred as confirmed with literature MD calculations for excess energy in a system due to precipitates [29]. The simulations confirmed that at sizes less than 10 nm, a Mo precipitate prefers an fcc structure within a Cu fcc matrix due to coherency stresses and reduced interfacial energy. From 10 to 20 nm, fcc and bcc Mo have equivalent energy penalties. Above 20 nm in size, bcc Mo precipitates are energetically favorable. Figure 6(c) shows a size dichotomy for the Mo precipitates in the 800°C film. The population of coarsened Mo precipitates revert to the equilibrium bcc phase while a number of smaller Mo precipitates remained in the fcc phase.

The HAADF STEM micrographs of Fig. 7 compare Cu-Ag and Mo-Ag deposited under identical processing conditions. The Cu and Ag formed equiaxed, Cu-rich and Ag-rich grains ~100 nm in size with equilibrium fcc phases [30]. The features of Cu-Ag resemble those of a similar Ni-Mo-W film which imply a random, soluble initial layer but later phase separation occurred as the deposition proceeded [31]. The Mo-Ag phase-separated into Ag-rich domains surrounded by an Ag-Mo LCM matrix. Both films had significant calculated $\Delta\rho$ values of 0.0159 for Cu-Ag and 0.0184 for Mo-Ag, showing quantitative inclination towards a heterogeneous morphology according to Fig. 2. The rationale for the homogeneity of the Cu-Ag and the heterogeneity of the Mo-Ag films lies in the T_H values which were $T_H^{\mathrm{Cu}} = 0.642$, $T_H^{\mathrm{Ag}} = 0.707$, and $T_H^{\mathrm{Mo}} = 0.301$. The disparity between T_H^{Mo} and T_H^{Ag} led to preferential agglomeration of Ag while the closeness of T_H^{Ag} and T_H^{Cu} resulted in concurrent equiaxed grain formation.

C. Hierarchical structures across multiple systems

Co-deposited Cu-Ta, Cu-Mo, Cu-Mo-Ag, and Mo-Ag films all presented hierarchical morphologies when fabricated

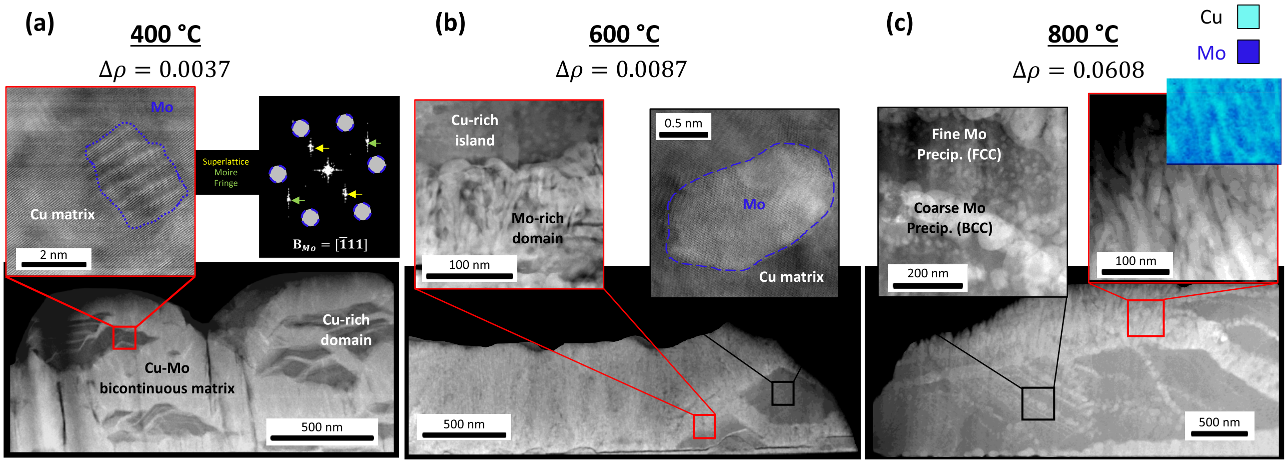

FIG. 6. Cu-Mo films fabricated at three distinct deposition temperatures (a) 400, (b) 600, (c) 800°C. STEM-HAADF imaging for all three films (bottom row for all three temperatures) with darker contrast regions that are Cu-rich and lighter contrast regions that are Cu-Mo bicontinuous matrix demonstrate hierarchical structures for each deposition with significant Cu-agglomerations containing trace Mo precipitates. The key difference between the three films is the organization of the Mo precipitates. Seen in the 400°C film (a), the Mo precipitates are ~ 5 nm in diameter and are organized in a superlattice structure as confirmed by fast Fourier transform (FFT). At 600°C (b) the Mo precipitates are approximately the same diameter but lose the superlattice structure. The Mo precipitates are noted to be in nonequilibrium fcc Mo phase. At 800°C (c), there is a size dichotomy in Mo precipitates with a population that is >20 nm in diameter and some ~ 10 nm in diameter. The smaller precipitates maintain the nonequilibrium phase while the larger are equilibrium fcc Mo. The energy dispersive x-ray spectroscopy (EDS) in (c) confirms the Cu-Mo bicontinuous matrix.

at an elevated deposition temperature, 600°C, and a reduced deposition rate, $\nu = 0.12$ nm/s. STEM-HAADF imaging in Fig. 8 shows a similar agglomeration-matrix/vein microstructure on the microscale with precipitate-matrix features on the nanoscale for the four alloys. We observed $\Delta\rho \geqslant 0.0087$ and $T_H \geqslant 0.35$ for at least one species but $T_H < 0.35$ for the remaining element(s).

The hierarchical architecture of the four systems can be juxtaposed by the scale on which the sample is observed. Cu-Ta in Fig. 8(a) portrays large Cu-rich agglomerates with a nonuniform interspersion of Ta precipitates in their equilibrium bcc phase. The Cu-rich agglomerates are surrounded by Ta-rich veins which lack any concentration modulations observed in the other three systems. Cu-Mo, as previously discussed in Fig. 6, displays Cu-rich agglomerates containing pseudomorphic fcc Mo precipitates all surrounded by Cu-Mo LCM matrix in Fig. 8(b). In the ternary alloy Cu-Mo-Ag, both Cu and Ag are considered highly mobile with similar surface interdiffusion lengths, $\rho = 120$ nm, and homologous temperatures, $T_H \geqslant 0.35$, in contrast to the immobile Mo, $\rho = 10$ nm. The Cu-Mo-Ag film in Fig. 8(c) depicts a microscopic Cu-rich agglomerate surrounded by a Mo-Ag RCM matrix. Nanoscale inhomogeneities are present in both the Cu-rich agglomerate and RCM matrix. Fine Mo- and Ag-rich clusters are observed in the Cu-rich region while spherical Ag-rich domains punctuate the RCM matrix. Last, Fig. 8(d) shows that the Mo-Ag system consists of Ag-rich domains encapsulated by a Mo-Ag LCM matrix. The nanoscopic features in Cu-Mo-Ag and Mo-Ag are in their equilibrium phases.

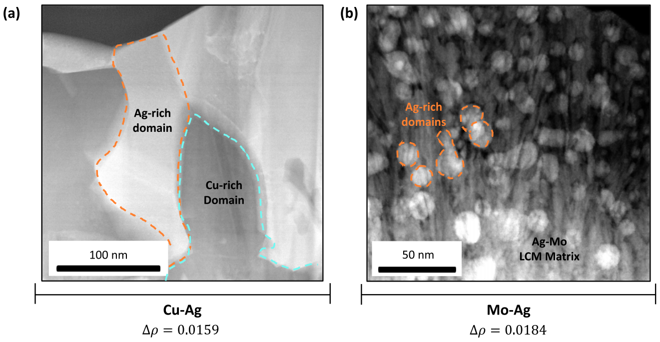

FIG. 7. STEM-HAADF micrographs of (a) Cu-Ag and (b) Mo-Ag deposited with the same processing parameters, $\nu = 1.4$ nm/s, temperature = 600 °C. The Cu-Ag has phase-separated into equiaxed Cu and Ag grains while the Mo-Ag displays the hierarchical structure. The significant $\Delta\rho$ in both cases indicates some additional kinetics influencing the formation of hierarchical architecture.

IV. DISCUSSION

The development of hierarchical morphologies presented in this work depends on the kinetics of thin film growth and the thermodynamics of immiscible systems. To deconvolve the underlying driving forces, it is pertinent to examine the phase-separation process for each length scale separately then combine them to understand the growth of the entire structure. First, the microscopic evolution will be examined to identify what induces the heterogeneous phase separation with simultaneous agglomeration and concentration modulation formation in hierarchical morphologies. Second, the energetics of nanoscale features will be discussed in the context of coherency stresses and interfacial energies to explain any metastable phases or lack thereof in the microstructure.

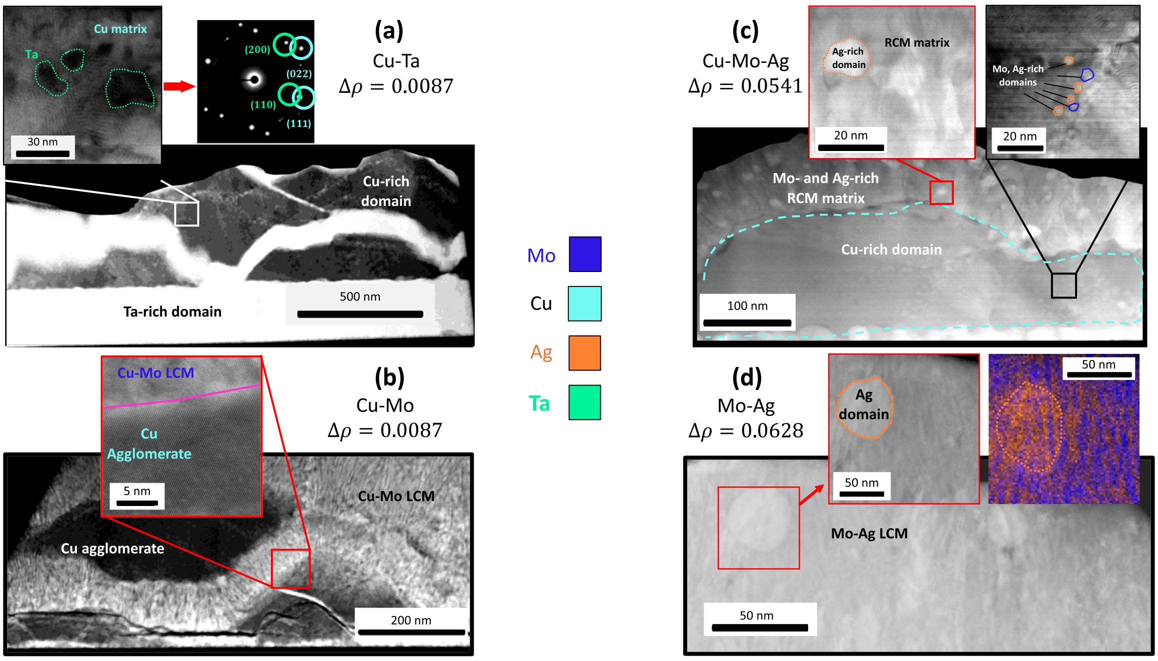

FIG. 8. STEM-HAADF image (larger images) of multiple systems presenting hierarchical morphologies for films deposited at $\nu = 0.15$ nm/s (Cu-Ta) and $\nu = 0.12$ nm/s (Cu-Mo, Cu-Mo-Ag, Mo-Ag), temperature = 600 °C. The immiscible alloys (a) Cu-Ta, (b) Cu-Mo, (c) Cu-Mo-Ag, and (d) Mo-Ag, have a range of $\Delta\rho$ values from 0.0087 to 0.0628 but all consistently display "structures composed of structures." Various insets of HR TEM micrographs (a)–(c), FFTs (a), and an EDS (d) image confirm the existence of features on multiple length scales for all four systems and suggests similar kinetic pathways during the formation process despite the variety of deposited species.

A. Primary microscopic phase separation

Equilibrium thermodynamics favor phase separation for all binary and ternary co-deposited samples discussed in this experiment [32]. Each set of elements was immiscible at the processing temperatures used during PVD. Thus, the comparative morphological variation across the six tested systems can be attributed to the film growth kinetics and constituent kinetic parameters of $\Delta\rho$ and T_H. The hierarchical structures were only noted in film processed with $\Delta\rho \geqslant 0.002$ while also containing at least one element with $T_H \geqslant 0.35$ and one element $T_H < 0.35$. As shown from Fig. 2 and Table I, these conditions only arise at reduced deposition rates and elevated temperatures. The result is a strong disparity in elemental mobility during deposition. Normally, once the landing adatoms reach the substrate surface they will phase-separate as described in the original model of Atzmon *et al.* [14]. In the conditions of significant elemental mobility difference, the highly mobile element will demix from the other element(s) and diffuse along the film surface into agglomerates during the deposition to reduce the interfacial energy between phase-separated regions. The less mobile element will diffuse relatively short distances before being buried and "frozen" by the oncoming deposition flux. The rapid agglomeration engulfs the less-mobile element which then become minority precipitates—a key characteristic of the hierarchical structures. Of interest is the phase fraction of the thin film and its influence on morphology. All the experimental binary alloys are 50-50 at.% as confirmed by XRF. However, as the highly mobile element agglomerates it induces localized regions of highly unequal phase fractions. Area image analysis shows the agglomerates and minority less-mobile element phase fraction ranges between 90-10 and 95-5 at.% which drive precipitate development. The remaining quantities which do not form the agglomerates and precipitates will concurrently phase-separate into concentration modulations or a veinlike structure as specifically noted in Cu-Ta of Fig. 8(a). The microscopic phase separation can be termed the "primary phase separation."

Figure 5 demonstrates the morphological sensitivity towards deposition rate and $\Delta\rho$ within the single Cu-Mo system. Although there is a consistent mobility difference for both depositions at 600°C as $T_H^{\mathrm{Cu}} = 0.642$ and $T_H^{\mathrm{Mo}} = 0.301$, a significant change in ν and a relatively small change in $\Delta\rho$ yielded distinct homogeneous and hierarchical microstructures. Increasing the deposition temperature and consequentially the elemental mobility difference in Fig. 6 led to the same general microscopic features. The higher temperature equated to greater Cu agglomeration and activates the bulk diffusion which allows coarsening of the Mo precipitates. Figure 7 proved that a system with $\Delta\rho \geqslant 0.0037$ requires the homologous temperature difference to yield a hierarchical structure. The Cu and Ag adatoms have approximately equal mobility with an equal propensity for agglomeration leading to the equiaxed Cu-Ag grains. In contrast, Ag-Mo had a $T_H^{\mathrm{Ag}} = 0.707$ and a $T_H^{\mathrm{Mo}} = 0.301$ resulting in Ag agglomerations and the characteristic heterogeneous microstructure.

Any *in situ* observation of the exact microscopic growth phenomena for hierarchical structures is complicated. Pausing the film deposition for a few minutes [9] or limiting the kinetic energy by depositing at room temperature [33] will yield amorphous or nanocrystalline phase-separated regions incomparable to the present experiment. Mesoscale modeling arises as the likely candidate for true comprehension of the polylithic heterogeneous architectures [34]. Coding frameworks have successfully replicated the formation of homogeneous morphologies in immiscible systems [17,35]. Other phase-field models have incorporated nonequilibrium oxide formation into phase separation during binary film growth [36]. However, a framework has yet to replicate the simultaneous multiscale evolution of hierarchical structures with appropriate scaling and both equilibrium and pseudomorphic phases present.

B. Secondary nanoscale phase separation

As established in the previous section, immiscible alloy vapor deposited films at elevated temperatures exhibit phase separation reaction on account of high enthalpy of mixing. The large disparity in mobilities of participating species and differing surface self-diffusivities have resulted in preferential agglomeration of one species and a microscopic mechanism leading to hierarchical structures shown comprehensively in Fig. 8.

Nanoprecipitates thus formed are observed to be uniformly interspersed in specific regions of the agglomerates. The nature of the precipitates reveals some important features. First, the atoms forming these precipitates belong to a species that is already chemically lean in the surrounding medium. Second, the medium in which these precipitates are embedded is an agglomerate that was formed earlier during primary phase separation reaction. Third, the precipitates share either coherent or semicoherent interface with the medium. Thin film studies on the Cu-W system synthesized by magnetron co-sputtering [9] linked interface coherency with spinodal-like modulations in self-assembled multilayered structures. Further, the size and distribution of precipitates indicate that the atoms involved in their formation traveled infinitesimally small distances to cluster locally and form several nanosized precipitates. This process is kinetically limited by the lower mobility of these atoms as the reaction occurs in the bulk where activation energies are significantly higher than that on the surface [37]. There is also a limited supply of these precipitate forming atoms because the medium in which they form is already compositionally lean in their respective species after having undergone primary phase separation reaction earlier. The very limited availability of atoms combined with a higher barrier to diffuse over significant distances results in small precipitate clusters interspersed inside the agglomerates.

The above observations suggest that in addition to primary phase separation reaction that enabled diffusion over long distances and allowed for initial agglomeration of highly mobile species, a possible secondary phase separation reaction that is akin to diffusionless transformation or a spinodal decay at a lesser degree is in the offing leading towards formation of nanoprecipitates. Typically, the phase separation in immiscible alloy system is represented by double-welled Gibbs' free energy curve with material flux chiefly via spinodal decomposition [38]. The underlying Gibb's equation combines enthalpy of mixing, ΔH, and entropy of mixing, ΔS, as

$$\Delta G = \Delta H - T\Delta S. \tag{5}$$

While the entropy curve by definition is concave upwards ($\Delta S = -R\sum x_i \ln x_i$, with x_i representing the population of a species), enthalpy acts as a strong factor in deciding the shape of the Gibb's curve. A strong, positive enthalpy of mixing gives rise to a double-welled Gibb's free energy curve of Eq. (5) with a localized maxima and two inflection points. This is especially true at elevated temperatures when the competition between enthalpy and entropy is equally strong in magnitude. Conventionally, enthalpy of mixing, ΔH_{mix}, is calculated using a simple linear model based on the following equation:

$$\Delta H_{\text{mix}} = H_{\text{mixture}} - \sum x_i H_i, \tag{6}$$

with H_{mixture} being the constant enthalpy of mixing, and $\sum x_i H_i$ is the summed product of energetics of the respective species. The resulting parabolic curve is similar to entropy but with opposite concavity. A more complex model for enthalpy of mixing involves a higher degree polynomial causing multiple maxima with corresponding inflection points in the Gibbs' free energy profile. In addition to this, the majority of the thermodynamic analysis is carried out assuming ideal conditions of thermodynamic equilibrium achieved in a reversible manner without restriction on kinetic aspects of phase separation. Any possible secondary or higher order phase separation reactions leading towards formation of metastable phases are often overlooked and difficult to capture when subjected to unique processing conditions like vapor deposition.

As the characterization in the present experiment occurred postdeposition, there is ambiguity that inhibits a definitive statement on the vehicle for secondary phase separation. Empirical evidence points to either a diffusionless transformation or a complex spinodal decomposition being the likely mechanisms for nanoprecipitate evolution. However, the exact nature of such spinodal decomposition is complicated by metastable phases and their implied complex Gibbs' free energy curve with additional local minima, $\frac{\partial G}{\partial c} = 0$, and multiple wells. Two phase ($\alpha + \beta$) Ti alloys provide some insight on nanostructure evolution as they have nanoscale features comparable to the current work [20]. The kinetic pathways and phase transitions in the Ti alloys are reliant on undercooling, the concentrations of existing composition, and processing pressures. The co-deposited immiscible alloys likely follow a similar dependency with different nonconventional processing conditions [39] emphasizing different pathways and leading to small nuances in the nanoscale evolution as evidenced in Fig. 6.

C. Pseudomorphism in nanoprecipitates

Metastable phases formed during growth are a consequence of material processing under forced constraints. While thermodynamics determines the potential for phase separation, vapor deposition techniques can kinetically limit this phase separation reaction by varying the flux of freshly deposited layers and by altering the substrate temperature either to suppress or enhance the mobility of participating atoms. Nanoprecipitates formed under such metastable conditions show pseudomorphic lattice structures in Cu-Mo and Cu-Ta systems as seen in Figs. 6 and 8.

Pseudomorphism has been studied extensively in thin films deposited by molecular beam epitaxy techniques where a deposited layer assumes the lattice structure corresponding to substrate that is different from bulk equilibrium structure. The ensuing coherent interface between deposited material and substrate results in elastic misfit strain and is sensitive to critical thickness of the deposited layer above which transition to bulk equilibrium structures is observed [40,41]. Contrastingly, the pseudomorphism observed in hierarchical structures is seen in precipitates that appear to have formed during secondary phase separation reaction by migrating and clustering locally inside an already agglomerated majority phase with lattice structures not observed in bulk equilibrium conditions.

Structural stability of these pseudomorphic nanoprecipitates incur an energy penalty during the formation of an interface and the associated pseudomorphic crystal structure. The interplay between surface-interface coherency [42] and system size [43] permits local minima in free energy corresponding to metastable pseudomorphic states accessible only with specific processing conditions. First-principles calculations by Aguayo *et al.* [44] on Ti, Zr, and Hf demonstrate the existence of a locally stable fcc structure based on elastic stability criteria. Analytical studies by Tomanek *et al.* [45] on the structural stability of nanosized clusters show close-packed fcc structures to be more stable than bulk bcc structure in metals like V, Nb, Cr, Mo, W, and Ta. Relating these studies to the present work, at early stages of precipitate formation there is a tendency towards close-packed fcc structure to align with the matrix-agglomerate material. As the precipitate size increases, it will undergo a martensitic transformation to bulk equilibrium bcc structure. Such transition is noted in the Cu-Mo system from Figs. 6(b) and 6(c). The transformation occurs at a critical size which is decided by the competition between precipitate-matrix interfacial energy and cohesive energy of the respective lattice structures at prevailing temperatures. Similar structural evolution has been reported in W nanoclusters during decomposition of W(CO)$_6$ vapors evolving from an amorphous to crystalline fcc structure before assuming a final bulk equilibrium bcc structure [46] with increasing cluster size.

The analytical model by Tomanek *et al.* [45] provides an energy-based criterion at which a cluster's lattice structure transforms from closed packed fcc to equilibrium bcc structure. Smaller clusters will have a higher proportional of surface atoms which contribute to high surface energy values. It is likely that the observed transformation in lattice structures is to minimize this surface energy and the condition for this transformation is given by the following equation [45]:

$$\frac{E_{\mathrm{bcc}} - E_{\mathrm{fcc}}}{E_{\mathrm{bcc}}} = \frac{1}{N}\left\{\sum_{i=1}^{N_s}\left[\left(\frac{Z_i}{Z_b}\right)^{1/2} - 1\right]_{\mathrm{fcc}} - \sum_{i=1}^{N_s}\left[\left(\frac{Z_i}{Z_b}\right)^{1/2} - 1\right]_{\mathrm{bcc}}\right\}, \quad (7)$$

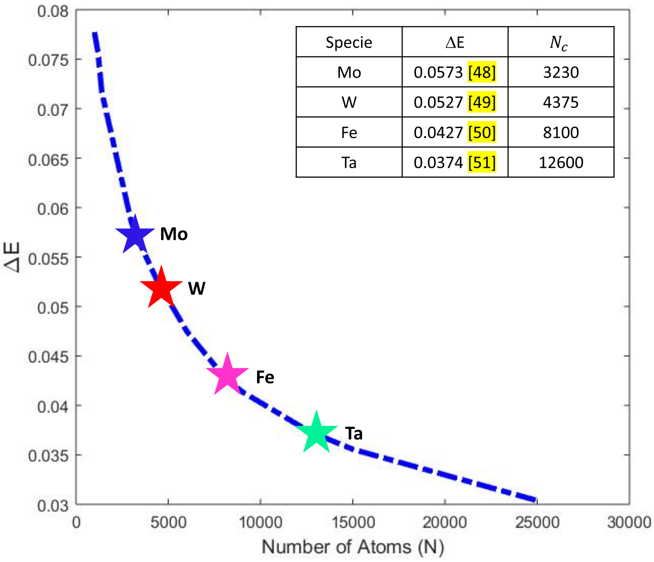

Specie	ΔE	N_c
Mo	0.0573 [48]	3230
W	0.0527 [49]	4375
Fe	0.0427 [50]	8100
Ta	0.0374 [51]	12600

FIG. 9. Analytically determined structural stability of nanoclusters depicting the critical number of atoms N_c at which the lattice structure shifts from close packed fcc to equilibrium bcc for select elements in accordance with Eq. (7). The vertical axis is normalized energy and the inset is a table which provides a general notion of critical cluster sizes for Mo and Ta seen in the hierarchical structures of the present micrographs [48–51].

where the left-hand side of the equation represented as ΔE in the Fig. 9 is the difference in formation energies between the bcc structure and the fcc structure normalized by the formation energy for bulk structure (bcc in this case). N and N_s represent the total number of atoms and number of surface atoms in the cluster, respectively. Z_i and Z_b refer to the coordination number of the i th atom and a bulk atom in the corresponding lattice, respectively. The summation on the right-hand side of the equation was individually computed for fcc and bcc structures by mapping surface atoms on spherical clusters and extracting coordination numbers data using LAMMPS [47] eventually resulting in the solid curve shown in Fig. 9. The above criterion is satisfied at a unique N value for each specie implying a critical number N_c of atoms required for the cluster to undergo structural transformation as indicated in Fig. 9. The critical cluster size for select elements is relevant or comparable to the current work, Mo, W, Fe, Ta, to highlight the phases seen experimentally.

Though the transformation from pseudomorphic structure to bulk equilibrium structure has been thoroughly established in theory and in experiments, the accuracy of the N_c is debatable and hard to capture in some species. This stems from the fact that the medium in which clusters and precipitates evolve strongly decides the surface-interface relationship which in turn influences the N_c. Furthermore, N_c will vary under nonequilibrium conditions of formation and growth where complex thermodynamic and kinetic factors are at play. Structural variations induced by stress, irradiation, electric/magnetic fields, vibrations, etc., in the process of microscopic examinations cannot be completely ruled out.

D. Morphology map for hierarchical structures

The present work can be summarized with two morphology maps of the empirically observed microstructures for the co-deposited immiscible alloy systems. The alloy systems are noted as forming homogeneous or hierarchical morphologies

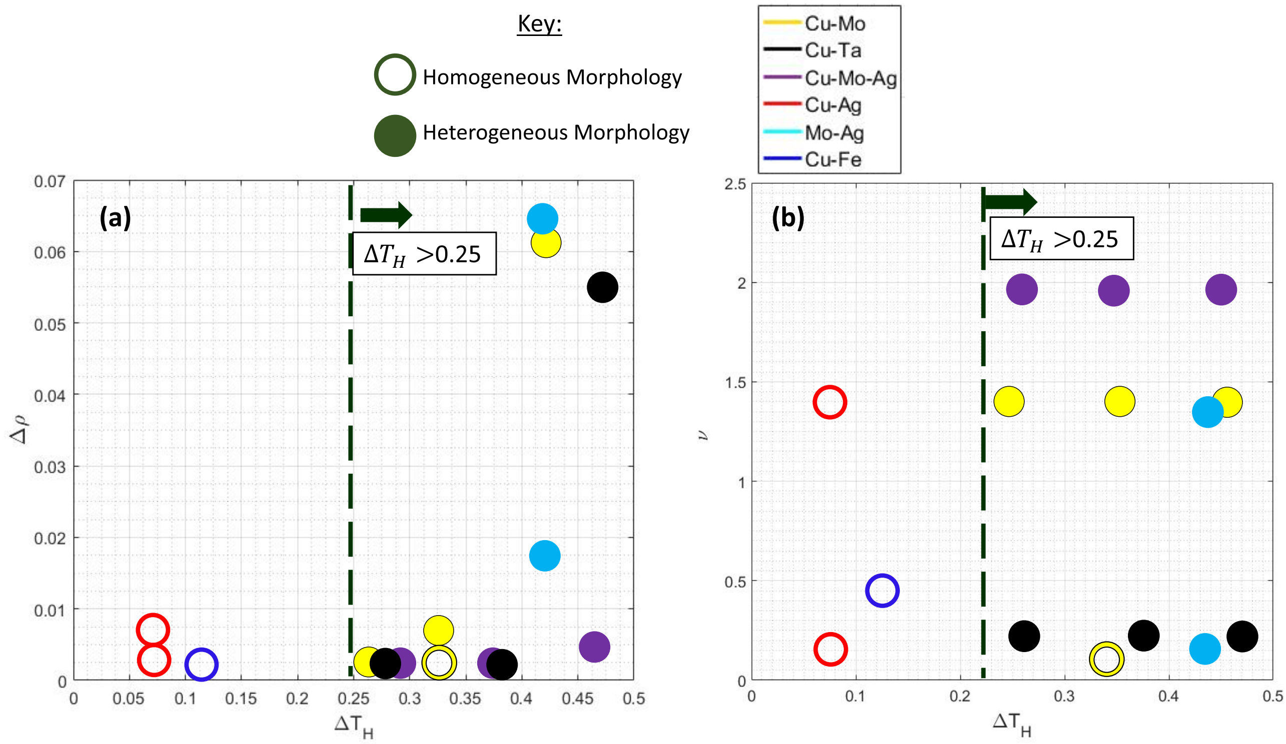

FIG. 10. (a) Morphology map with the variables $\Delta\rho$ and ΔT_H, the difference in homologous temperature of the constituent species. The empirically observed morphologies of the experimentally deposited systems are plotted as a function of their processing conditions. Two resultant groupings are noted. First, only heterogeneous morphologies were present at $\Delta\rho > 0.01$. Second, with $\Delta\rho < 0.01$, any systems with $\Delta T_H < 0.25$ yielded homogeneous morphologies. (b) Second morphology map with ν and ΔT_H. At the low deposition rates probed in this experiment, the ΔT_H has significantly higher influence on the resultant microstructure morphology. The dashed vertical lines indicate the $\Delta T_H > 0.25$ in both maps (a) and (b) which appears to be the threshold for homogeneous vs heterogeneous architectures except for the single Cu-Mo sample deposited at 600°C.

as a function of processing kinetics in the maps of Figs. 10(a) and 10(b). The resultant morphologies of the experimental systems are plotted with respect to the kinetic parameters, the comparative homologous temperature ΔT_H, and the difference in surface interdiffusion length $\Delta\rho$ for Fig. 10(a) and for deposition rate ν and ΔT_H for Fig. 10(b). The comparative homologous temperature is evaluated as the difference in T_H for the constituent elements (taken as the average difference in Cu-Mo-Ag). The ΔT_H is selected due to the characterization of Cu-Fe in Fig. 3 and Cu-Ag in Fig. 7 which indicate that the relative difference in constituent homologous temperature is critical to preferential agglomeration of one species and thus heterogeneous morphologies.

Figures 10(a) and 10(b) show that no single kinetic parameter can be directly correlated to the heterogeneous microstructure. Instead, all three parameters, $\Delta\rho$, ν, and ΔT_H, contribute to hierarchical formation. The ΔT_H is the most significant driver since the homogeneous microstructures are directly correlated to low ΔT_H values. At the threshold $\Delta T_H > 0.25$, noted as dotted lines in Figs. 10(a) and 10(b), the co-deposited immiscible alloys yielded hierarchical structures in all cases but one. Figure 7 indicated that the kinetic parameter $\Delta\rho$ can still be affiliated with one element having sufficient kinetic energy to preferentially agglomerate to engulf the immobile complementary element and initiate the multimodal formation. However, Fig. 10(a) reveals that the threshold $\Delta\rho$ value is likely quite low and must be paired with elevated ΔT_H for hierarchical self-assembly. The deposition rate ν has a significant influence on morphology when examined across a large range of rates. This was noticed in Fig. 5 with a change in morphology as ν increased by an order of magnitude from Figs. 5(a) to 5(b). However, the present experiment probed ν across a range of very low to low values, 0.12–2 nm/s, which reduced the prominence of the deposition rate and its effect on surface interdiffusion lengths. Increasing ν to medium or high rates would limit the surface interdiffusion length of all deposited species and suppress heterogenous structures. While the present study examines six co-deposited immiscible systems, the trends apparent in Figs. 10(a) and 10(b) may be predictive of the morphologies in a number of deduced immiscible alloy systems adding another dimension to alloy maps as mentioned by Zhang *et al.* [52].

V. CONCLUSIONS

Experimental micrographs and energetic theory combine to present a comprehensive description of hierarchical structures in co-sputtered immiscible alloys and their formation mechanisms concurrent on the microscopic and nanoscales. The hierarchical structures have a primary and secondary phase separation occurring simultaneously with the pathway:

(1) At the microscopic level, the primary phase separation at the processing conditions of low deposition rates and elevated deposition temperatures induce the landing adatoms of the one species with significant surface diffusivity to agglomerate to reduce the energy of the system. The agglomeration will trap a trace amount of the second species which becomes nanoprecipitates. The remaining material for both species will form concentration modulations that will surround the agglomerates.

(2) At the nanoscale, the nanoprecipitates will evolve according to the secondary phase separation. Longer deposition times and increased temperature incentivize bulk diffusion which will coarsen the microstructure. The nanoprecipitates likely evolve via a diffusionless transformation or complex spinodal decomposition, sometimes occupying a pseudomorphic state then transitioning to their bulk equilibrium state as they become larger in size.

The above steps are relevant for co-deposited immiscible systems which phase-separate into distinct regions. Furthermore, the hierarchical structures will only develop under specific kinetics with high T_H values, low ν, and significant $\Delta\rho$ for the alloy.

ACKNOWLEDGMENTS

The authors would like to acknowledge Professor M. Demkowicz of Texas A&M University for the scientific discussion of the fundamental phenomena pertinent to this work. Mesoscale modeling concepts were developed in collaboration with the Center for Integrated Nanotechnologies (CINT) with the assistance of Dr. R. Dingreville and Dr. J. Stewart. This research was performed under the Center for Research Excellence on Dynamically Deformed Solids (CREDDS) sponsored by the Department of Energy – National Nuclear Security Administration (DOE-NNSA), Stewardship Science Academic Program under Award No. DE-NA0003857. Microscopy was performed at the Michigan Center for Materials Characterization at the University of Michigan and at Northwestern University under the Northwestern University Atomic and Nanoscale Characterization Experimental Center in the Electron Probe Instrumentation Center. Computation and theoretical work utilized the Great Lakes High Performance Computation Cluster of the University of Michigan.

M.P. and B.D. contributed equally.

[1] R. Lakes, Materials with structural hierarchy, Nature **361**, 511 (1993).

[2] P. Braun and R. Nuzzo, Knowing when small is better, Nat. Nanotechnol. **9**, 962 (2014).

[3] A. Chen, Q. Su, H. Han, E. Enriquez, and Q. Jia, Metal oxide nanocomposites: A perspective from strain, defect, and interface, Adv. Mater. **31**, 1803241 (2019).

[4] Q. Li, S. Xue, P. Price, X. Sun, J. Ding, Z. Shang, Z. Fan, H. Wang, Y. Zhang, Y. Chen, H. Wang, K. Hattar, and X. Zhang, Hierarchical nanotwins in single-crystal nickel with high strength and corrosion resistance produced via a hybrid technique, Nanoscale **12**, 1356 (2020).

[5] Y. Cui, B. Derby, N. Li, N. A. Mara, and A. Misra, Suppression of shear banding in high-strength Cu/Mo nanocomposites with hierarchical bicontinuous intertwined structures, Mater. Res. Lett. **6**, 184 (2017).

[6] Y. Cui, B. Derby, N. Li, and A. Misra, Fracture resistance of hierarchical Cu-Mo nanocomposite thin films, Mater. Sci. Eng. A **799**, 139891 (2021).

[7] B. Derby, J. K. Baldwin, D. Chen, M. Demkowicz, Y. Wang, A. Misra, and N. Li, Faceted He-filled "pancakes" confined within nanoscale metal layers, JOM **72**, 145 (2020).

[8] B. Derby, Y. Cui, J. K. Baldwin, R. Arroyave, M. Demkowicz, and A. Misra, Processing of novel psuedomorphic Cu-Mo hierarchies in thin films, Mater. Res. Lett. **7**, 1 (2019).

[9] T. Xie, L. Fu, W. Qin, J. Zhu, W. Yang, D. Li, and L. Zhou, Self-assembled metal nano-multilayered film prepared by co-sputtering method, Appl. Surf. Sci. **435**, 16 (2018).

[10] J. Xue, Y. Li, L. Hao, L. Gao, D. Qian, Z. Song, and J. Chen, Investigation on the interfacial stability of multilayered Cu-W films at elevated deposition temperatures during co-sputtering, Vacuum **166**, 162 (2019).

[11] A. Bahrami, C. F. Onofre Carrasco, A. Delgado Cardona, T. Huminiuc, T. Polcar, and S. E. Rodil, Mechanical properties and microstructural stability of CuTa/Cu composite coatings, Surf. Coat. Technol. **364**, 22 (2019).

[12] C. M. Muller, A. Sologubenko, S. Gerstl, and R. Spolenak, On spinodal decomposition in Cu-34 at.% Ta thin films - an atom probe tomography and transmission electron microscopy study, Acta Mater. **89**, 181 (2015).

[13] B. Derby, Y. Cui, J. K. Baldwin, and A. Misra, Effects of substrate temperature and deposition rate on the phase separated morphology of co-sputtered, Cu-Mo thin films, Thin Solid Films **647**, 50 (2018).

[14] M. Atzmon, D. A. Kessler, and D. Srolovitz, Phase separation during film growth, J. Appl. Phys. **72**, 442 (1992).

[15] C. Adams, M. Atzmon, Y. T. Cheng, and D. Srolovitz, Phase separation during co-deposition of Al-Ge thin films, J. Mater. Res. **7**, 653 (1992).

[16] J. Thornton, Influence of apparatus geometry and deposition conditions on the structure and topography of thick sputtered coatings, J. Vac. Sci. Technol. **11**, 666 (1974).

[17] A. Kumar, B. Derby, R. Raghavan, A. Misra, and M. Demkowicz, 3-D phase-field simulations of self-organized composite morphologies in physical vapor deposited phase-separating binary alloys, J. Appl. Phys. **126**, 075306 (2019).

[18] J. Stewart and R. Dingreville, Microstructure morphology and concentration modulation of bicontinuous nanocomposite thin-films during simulated physical vapor deposition, Acta Mater. **188**, 181 (2020).

[19] Y. Lu, C. Wang, Y. Gao, R. Shi, X. Liu, and Y. Wang, Microstructure Map for Self-Organized Phase Separation during Film Deposition, Phys. Rev. Lett. **109**, 086101 (2012).

[20] T. W. Heo, D. Shih, and L. Q. Chen, Kinetic pathways of phase transformations in two-phase Ti alloys, Metall. Mater. Trans. A **45**, 3438 (2014).

[21] M. Powers, B. Derby, A. Shaw, E. Raeker, and A. Misra, Microstructural characterization of phase-separated co-deposited

Cu-Ta immiscible alloy thin films, J. Mater. Res. **35**, 1531 (2020).

[22] C. Adams and D. Srolovitz, Monte carlo simulations of phase separation during thin-film codeposition, J. Appl. Phys. **74**, 1707 (1993).

[23] F. T. Vullers and R. Spolenak, From solid solutions to fully phase separated interpenetrating networks in sputter deposited “immiscible” W-Cu thin films, Acta Mater. **99**, 213 (2015).

[24] C. M. Muller, S. Parviainen, F. Djurabekova, K. Nordlund, and R. Spolenak, The as-deposited structure of co-sputtered Cu-Ta alloys, studied by X-ray diffraction and molecular dynamics simulations, Acta Mater. **82**, 51 (2015).

[25] S. L. Lee, M. Doxbeck, J. Mueller, M. Cipollo, and P. Cote, Texture, structure, and phase transformation in sputter beta tantalum coating, Surf. Coat. Technol. **178**, 44 (2004).

[26] K. Fukutani, K. Tanji, T. Saito, and T. Den, Fabrication of well-aligned Al nanowire array embedded in Si matrix using limited spinodal decomposition, Jpn. J. Appl. Phys. **47**, 1140 (2008).

[27] M. Ohring, *Materials Science of Thin Films: Deposition and Structure* (World Scientific, San Diego, California, 2002).

[28] P. Sidles and G. Danielson, Thermal diffusivity of metals at high temperatures, J. Appl. Phys. **25**, 58 (1954).

[29] A. van de Walle, M. Asta, and G. Ceder, The alloy theoretic automated toolkit: A user guide, Comput. Coupling Phase Diagrams Thermochem. **26**, 539 (2002).

[30] S. Gohil, R. Banerjee, S. Bose, and P. Ayyub, Influence of synthesis conditions on the nanostructure of immiscible copper-silver alloy thin films, Scr. Mater. **58**, 842 (2008).

[31] G. D. Sim, J. Krogstad, K. Xie, S. Dasgupta, G. Valentino, T. Weihs, and K. Hemker, Tailoring the mechanical properties of sputter deposited nanotwinned nickel-molybdenum-tungsten films, Acta Mater. **144**, 216 (2018).

[32] H. Okamoto, Phase diagrams for binary alloys, in *Desk Handbook*, 2nd ed., edited by H. Okamoto, T. Massalski, P. Subramanian, and L. Kacprzak (ASM International, Materials Park, Ohio, 2000), p. 307.

[33] K. Asami, T. Moriya, K. Hashimoto, and T. Masumoto, Roles of temperature and humidity in the oxidation of sputter-deposited Cu-Ta alloys in air, Corros. Sci. **44**, 331 (2002).

[34] E. Herman, J. Stewart, and R. Dingreville, A data-driven surrogate model to rapidly predict microstructure morphology during physical vapor deposition, Appl. Math. Model. **88**, 589 (2020).

[35] L. Q. Chen, Phase-field models for microstructure evolution, Annu. Rev. Mater. Res. **32**, 113 (2002).

[36] G. Kairaitis and A. Galdikas, Mechanisms and dynamics of layered structure formation during co-deposition of binary compound thin films, Coatings **10**, 21 (2020).

[37] *Smithells Metals Reference Book*, 8th ed., edited by T. C. Totemeier and W. F. Gale (Elsevier Butterworth-Heinemann, Burlington, MA), Chap. 13.

[38] J. Z. Zhao, T. Ahmed, H. X. Jiang, J. He, and Q. Sun, Solidification of immiscible alloys: A review, Acta Metall. Sin. (Engl. Lett.) **30**, 1 (2017).

[39] W. A. Soffa and D. E. Laughlin, Decomposition and ordering processes involving thermodynamically first order order-disorder transformations, Acta Metall. **37**, 3019 (1998).

[40] J. H. van der Merwe, Equilibrium structure of a thin epitaxial film, J. Appl. Phys. **41**, 4725 (1970).

[41] W. A. Jesser, A theory of pseudomorphism in thin films, Mater. Sci. Eng. **4**, 279 (1969).

[42] S. A. Dregia, R. Banerjee, and H. L. Fraser, Polymorphic phase stability in thin multilayers, Scr. Mater. **39**, 217 (1998).

[43] E. B. Dolgusheva and V. Y. Trubitsyn, Molecular dynamics investigation of the structural stability of body-centered cubic zirconium nanofilms, Phys. Solid State **54**, 1652 (2012).

[44] A. Aguayo, G. Murrieta, and R. de Coss, Elastic stability and electronic structure of fcc Ti, Zr, and Hf: A first-principles study, Phys. Rev. B **65**, 092106 (2002).

[45] D. Tomanek, S. Mukherjee, and K. H. Bennemann, Erratum: Simple theory for the electronic and atomic structure of small clusters, Phys. Rev. B **29**, 1076 (1984).

[46] S. J. Oh, S. H. Huh, H. K. Kim, J. W. Park, and G. H. Lee, Structural evolution of W nano clusters with increasing cluster size, J. Chem. Phys. **111**, 7402 (1999).

[47] S. Plimpton, Fast parallel algorithms for short-range molecular dynamics, J. Comput. Phys. **117**, 1 (1995); http://lammps.sandia.gov.

[48] H. Park, M. R. Fellinger, T. J. Lenosky, W. W. Tipton, D. R. Trinkle, S. P. Rudin, C. Woodward, J. W. Wilkins, and R. G. Hennig, Ab initio based empirical potential used to study the mechanical properties of molybdenum, Phys. Rev. B **85**, 214121 (2012).

[49] M. Marinica, L. Ventelon, M. Gilbert, L. Proville, S. Dudarev, J. Marian, G. Bencteux, and F. Willaime, Interatomic potentials for modelling radiation defects and dislocations in tungsten, J. Phys.: Condens. Matter **25**, 395502 (2013).

[50] L. Malerba, M. Marinica, N. Anento, C. Björkas, H. Nguyen, C. Domain, F. Djurabekova, P. Olsson, K. Nordlund, A. Serra, D. Terentyev, F. Willaime, and C. Becquart, Comparison of empirical interatomic potentials for iron applied to radiation damage studies, J. Nucl. Mater. **406**, 19 (2010).

[51] G. Pun, K. Darling, L. Kecskes, and Y. Mishin, Angular-dependent interatomic potential for the Cu-Ta system and its application to structural stability of nano-crystalline alloys, Acta Mater. **100**, 377 (2015).

[52] R. F. Zhang, X. F. Kong, H. T. Wang, S. H. Zhang, D. Legut, S. H. Sheng, S. Srinivasan, K. Rajan, and T. C. Germann, An informatics guided classification of miscible and immiscible binary alloy systems, Sci. Rep. **7**, 9577 (2017).